

# Lateral NbS<sub>2</sub>/MoS<sub>2</sub>/NbS<sub>2</sub> transistors: physical modeling and performance assessment

Giuseppe Lovarelli,<sup>1,2,\*</sup> Fabrizio Mazziotti,<sup>2,†</sup> Demetrio Logoteta,<sup>3,‡</sup> and Giuseppe Iannaccone<sup>2,§</sup>

<sup>1</sup>*Dipartimento di Fisica, Università di Pisa, Largo Bruno Pontecorvo 3, 56127 Pisa, Italy*

<sup>2</sup>*Dipartimento di Ingegneria dell'Informazione, Università di Pisa, Via Caruso 16, 56122 Pisa, Italy*

<sup>3</sup>*Dipartimento di Ingegneria dell'Informazione, Elettronica e Telecomunicazioni, Università di Roma La Sapienza, via Eudossiana 18, 00184, Roma, Italy*

Reducing the contact resistance of field-effect transistors based on two-dimensional materials is one of the key improvements required to enable the integration of such transistors in an industrially relevant process. Suitably designed lateral heterojunctions provide an opportunity to independently tailor the contact and channel properties and to mitigate the problem of high contact resistance. Inspired by the recent experimental demonstration of a two-dimensional *p*-type Schottky barrier, here we use quantum transport simulations to estimate the performance of *p*-type transistors in which the channel consists of a lateral heterostructure of NbS<sub>2</sub>/MoS<sub>2</sub>/NbS<sub>2</sub> (semimetal-semiconductor-semimetal). We find that the gate alignment with the channel is a critical design parameter, strongly influencing the capability of the gate to modulate the Schottky barrier at the MoS<sub>2</sub>/NbS<sub>2</sub> interfaces. This effect is also found to significantly affect the scaling behavior of the device.

## I. INTRODUCTION

The possibility of using two-dimensional (2D) materials in an industrially relevant CMOS process depends on a few factors, among which the capability to fabricate low-resistance metal contacts is critical. Unfortunately, 2D semiconductors tend to form high Schottky barriers with bulk metals, and the difficulty in achieving high doping levels in monolayers hinders the adoption of the conventional approach based on thinning these barriers enough to make them transparent to carrier tunnelling [1–3].

Contacting semiconducting monolayers by defining vertical or lateral heterojunctions with 2D material-based metals has been attracting significant interest [4–11], especially in the perspective of developing all-2D circuits where every circuit component, including metallizations and insulating regions, is based on 2D materials.

In vertical heterojunctions, monolayers are weakly coupled by van der Waals interactions. This prevents the undesired occurrence of interfacial spurious states and Fermi level pinning [1, 12–14]; however, the small coupling also entails low carrier injection [13]. On the other hand, the edge contact between monolayers in lateral heterojunctions is characterized by a stronger coupling due to the covalent character of the atomic bonds. Provided that the quality of the interface is controlled and the height of the Schottky barrier is low enough, this translates to potentially efficient carrier injection [15, 16].

The capability to engineer both *n*- and *p*-type contacts is another essential requirement to implement a CMOS technology. Unfortunately, realizing *p*-type FETs based on 2D materials has proven extremely challenging, due to the strong influence of the commonly used dielectric substrates, that tend to induce an *n*-type doping in the channel and of Fermi level pinning at the conduction band [17].

In this respect, recent experiments have demonstrated the fabrication of *p*-type Schottky diodes based on a lateral heterojunction of NbS<sub>2</sub> and MoS<sub>2</sub> [18]. The reported, significant, current modulation indicates an effective reduction of the parasitic resistance associated to the MoS<sub>2</sub> contact when the NbS<sub>2</sub> buffer region is included. Considering some critical parameters extracted from Ref. [18] and by means of quantum transport simulations, in this paper we study the physics and the upper performance limit of a *p*-type field-effect transistor based on a monolayer MoS<sub>2</sub> channel connected to monolayer NbS<sub>2</sub> access regions through lateral heterojunctions. Our results indicate that the phonon-assisted interband tunnelling at the NbS<sub>2</sub>/MoS<sub>2</sub> interfaces plays a major role in determining the device behavior. It also translates into a pronounced sensitivity of the device to some architectural details, such as the alignment between the gate electrode and the channel, that should be carefully addressed in order to optimize its performance.

The paper is organized as follows. In Section II, we present our model and simulation strategy. In Section III, we discuss our results in terms of the device physics, performance and optimization opportunities. Our concluding remarks are drawn in Section IV.

## II. MODEL

Following Ref. [18], we model the isolated monolayers by means of the two-bands first-nearest neighbor tight-binding Hamiltonian

$$H_{2D,j}(\mathbf{k}) = \begin{pmatrix} E_{0,j} & t_j f_{2D}(\mathbf{k}) \\ t_j^* f_{2D}^*(\mathbf{k}) & E_{0,j} + E_G \end{pmatrix}, \quad (1)$$

where  $j = (\text{MoS}_2, \text{NbS}_2)$ , for MoS<sub>2</sub>,  $E_G$  is the energy gap and  $E_0$  is the maximum energy of the valence band, while the minimum of the NbS<sub>2</sub> band that couples with it is given by  $E_0 + E_G$ . Moreover,  $t$  is the hopping parameter and

$$f_{2D}(\mathbf{k}) = 1 + 2 \cos\left(\frac{a}{2}k_x\right) e^{i\frac{\sqrt{3}}{2}k_y} \quad (2)$$

\* giuseppe.lovarelli@phd.unipi.it

† f.mazziotti@phd.unipi.it

‡ demetrio.logoteta@uniroma1.it

§ giuseppe.iannaccone@unipi.it

TABLE I: Tight-binding parameters and deformation potentials used in simulations

$E_{G,NbS_2}$	5.25 eV
$E_{G,MoS_2}$	2.10 eV
$E_{0,MoS_2}$	-0.17 eV
$t_{NbS_2}$	-0.91 eV
$t_{MoS_2}$	-1.20 eV
$\hbar\omega_{ph}$	0.05 eV
$D_{op}$	$4.6 \times 10^8$ eV/cm
$D_{ac}$	2.5 eV

is the Bloch function describing the periodicity of the hexagonal lattice. In agreement with the experimental and theoretical analyses in [18], the MoS<sub>2</sub>-NbS<sub>2</sub> band alignment was set in order to fulfill the constraint  $E_{0,MoS_2} - \mu_{NbS_2} = 0.17$  eV, where  $\mu_{NbS_2}$  is the electrochemical potential at the NbS<sub>2</sub> contacts. The interface between the monolayers is assumed defectless (see Fig. 1) and the hopping  $t_{IF}$  between NbS<sub>2</sub> sulphur atoms and MoS<sub>2</sub> molybdenum atoms is assumed equal to  $t_{NbS_2}$ . Due to the closeness between the values of  $t_{MoS_2}$  and  $t_{NbS_2}$ , no significant differences are expected by setting  $t_{IF}$  to  $t_{NbS_2}$  or to an intermediate value between  $t_{MoS_2}$  and  $t_{NbS_2}$ . We report the parameters of the model in Table I.

Transport simulations were performed within the non-equilibrium Green's function formalism [19]. An orthorhombic elementary cell is designated to describe the system in real space in the direction of transport, and the device is assumed periodic in the lateral direction orthogonal to it. To sample the Brillouin zone along this transverse direction, a set of 100 transverse wave vectors were taken into account in simulations. In order to obtain a self-consistent solution, the transport equations were nonlinearly coupled with the 2D Poisson equation in the device cross section. The resulting system of equations was iteratively solved by adopting a fixed-point approach. Convergence was considered achieved when the maximum difference between the potential energy profile in consecutive iterations was less than 1 meV.

Electron-phonon scattering was included in the transport equations within the self-consistent Born approximation through diagonal self-energies [20] and by assuming an elastic and dispersionless approximation for acoustic and optical phonons, respectively. The optical phonon energy was obtained as the arithmetical average of the longitudinal, transverse and homopolar optical branches in MoS<sub>2</sub>, and set to  $\hbar\omega = 50$  meV [21]. Hole-phonon coupling was modeled within the deformation potential approximation, by only considering the intravalley hole scattering at the  $K$  point [22]. The values of the acoustic and optical deformation potentials ( $D_{op}$  and  $D_{ac}$ , respectively) are reported in Table I.

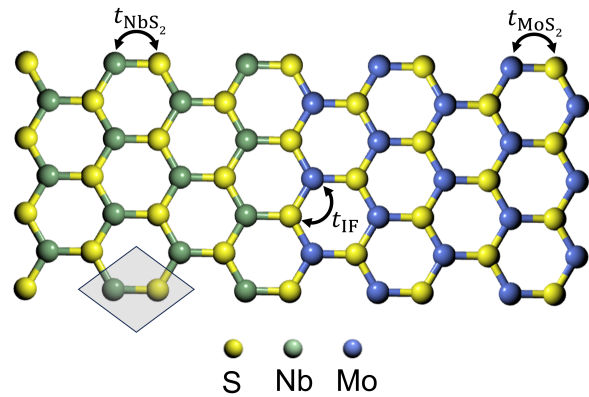


FIG. 1: Sketch of the MoS<sub>2</sub>/NbS<sub>2</sub> heterointerface. The shaded region depicts the unit cell of the lattice. The tight-binding parameters are also indicated.

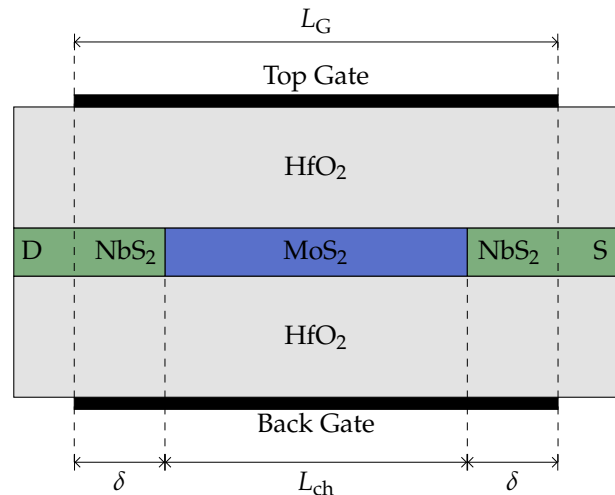


FIG. 2: Sketch of the cross section of the NbS<sub>2</sub>/MoS<sub>2</sub>/NbS<sub>2</sub> transistor.

### III. RESULTS AND DISCUSSION

The cross-section of the NbS<sub>2</sub>/MoS<sub>2</sub>/NbS<sub>2</sub> transistor is sketched in Fig. 2. The current flow is controlled by means of a top and a bottom gate, separated from the channel by a 3.4 nm-thick HfO<sub>2</sub> layer with relative permittivity  $\epsilon_r = 20$ . The gate length  $L_G$  can be larger or smaller than the MoS<sub>2</sub> channel length  $L_{ch}$ ; this difference is quantified by the algebraic parameter  $\delta = (L_G - L_{ch})/2$ . The NbS<sub>2</sub> source (S) and drain (D) extensions are 12 nm long. According to the estimates in Ref. [18], the MoS<sub>2</sub> channel is  $p$ -doped at a concentration  $6 \times 10^{12}$  cm<sup>-2</sup>.

Fig. 3a illustrates the transfer characteristics of the transistor for  $L_{ch} = 20$  nm,  $\delta = 0$  and different values of  $V_{DS}$ . A pronounced maximum of the current is observed, that shifts towards more negative  $V_{GS}$  as  $|V_{DS}|$  increases. This effect can be explained with the help of Fig. 3b, that reports the band diagram of the transistor (central panel)

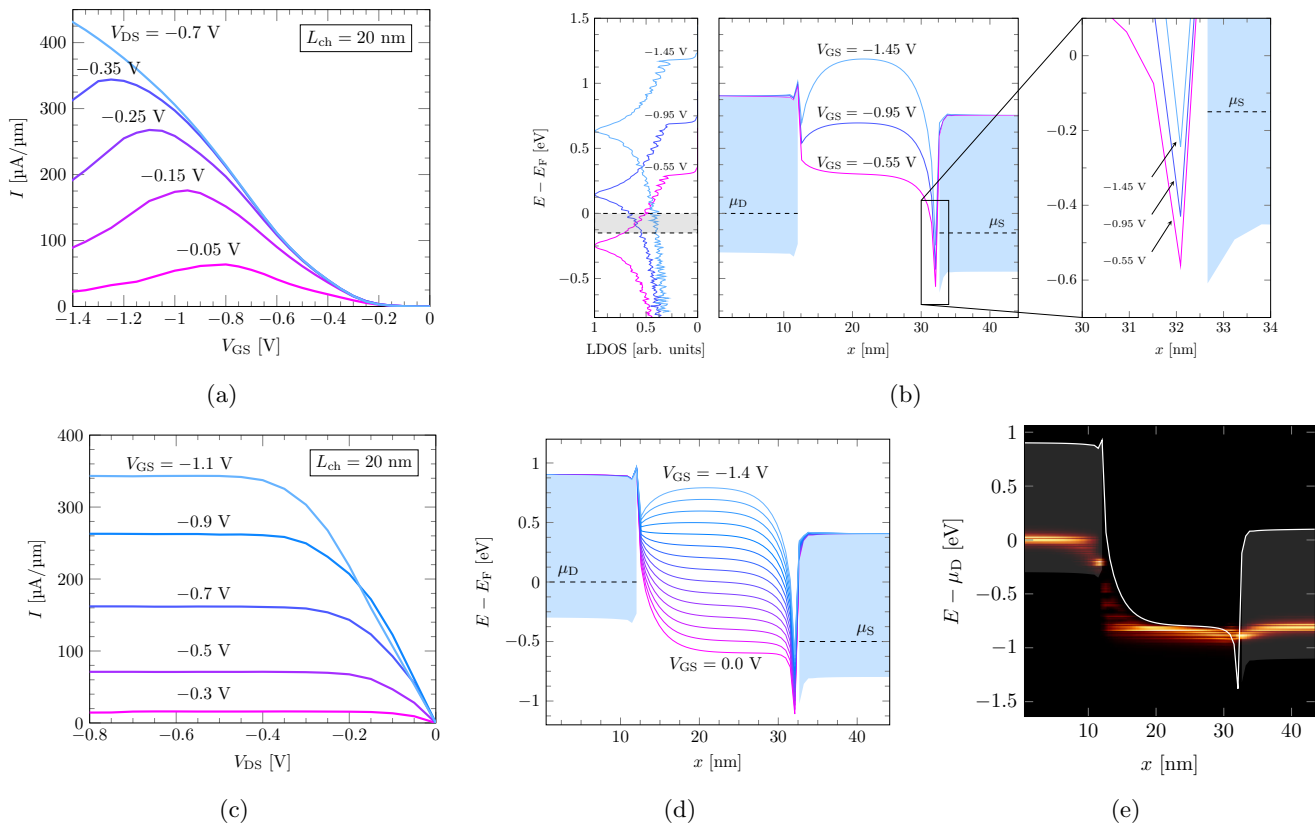


FIG. 3: (a) Transistor transfer characteristics for different values of  $V_{\text{DS}}$ . (b) Band diagram along the device (center panel) and local density of states in the center of the channel (left panel) at  $V_{\text{DS}} = -0.15$  V and for three  $V_{\text{GS}}$  values close to the current peak. The blue-colored regions cover the energy window of the NbS<sub>2</sub> band involved in transport. The right panel is an enlargement of the band diagram close to the channel/source interface. (c) Transistor output characteristics. (d) Band diagram along the device for several values of  $V_{\text{GS}}$ . (e) Current spectrum at  $V_{\text{DS}} = -0.8$  V and  $V_{\text{GS}} = 0.1$  V. For all the panels,  $L_{\text{ch}} = 20$  nm.

for  $V_{\text{DS}} = -0.15$  V and three values of  $V_{\text{GS}}$ , located before, at, and after the current peak. The corresponding local density of states (LDOS) in the middle of the channel is shown in the left panel of the figure, while the right panel presents a magnified view of the band diagram close to the MoS<sub>2</sub>/NbS<sub>2</sub> interface at the source. The LDOS exhibits a peak, corresponding to the local flattening of the MoS<sub>2</sub> valence band at the  $M$  point. The current is mainly limited by two factors: the density of available states in the channel between the source and drain electrochemical potentials (grey stripe in Fig. 3b), and the width of the tunneling barrier at the channel-drain interface. As the gate voltage is swept through the current peak, the barrier thins, while the density of states decreases. The competition between the two phenomena induces the current peak.

When the absolute value of  $V_{\text{DS}}$  increases, the tunneling barrier at the source/channel interface at a given energy widens. As a consequence, more negative gate voltages are needed to reach the current peak.

At  $V_{\text{DS}} = -0.8$  V and  $-0.6$  V, the  $I_{\text{ON}}/I_{\text{OFF}}$  ratio equals 2330 and 1290, respectively. These values are obtained by setting  $I_{\text{OFF}} = 0.1 \mu\text{A}/\mu\text{m}$  [23] and computing

$I_{\text{ON}}$  at  $V_{\text{GS}} = V_{\text{GS,OFF}} + V_{\text{DS}}$ , where  $V_{\text{GS,OFF}}$  is the gate voltage at which  $I_{\text{D}} = I_{\text{OFF}}$ . We maintain these definitions through the paper.

The output characteristics of the transistor with  $L_{\text{ch}} = 20$  nm are reported in Fig. 3c. An excellent current saturation at large bias is observed. Furthermore, we can observe that at low  $|V_{\text{DS}}|$  the curve at  $V_{\text{GS}} = -1.1$  V intersects with the curve at lower  $V_{\text{GS}}$ . This is simply due to the presence of the peak in the  $I - V_{\text{GS}}$  characteristics showed in Figure 3b. Fig. 3d shows the band diagram along the device for several values of  $V_{\text{GS}}$ , which confirms an almost perfect electrostatic control of the gate over the channel potential, corresponding to a gate efficiency  $\partial E_{\text{v}}/\partial V_{\text{GS}} \approx 0.98$ , where  $E_{\text{v}}$  is the top of the valence band at the center of the channel.

Despite this almost ideal electrostatic control of the gate over the channel, the subthreshold swing of the device is about 95 mV/dec and is thus degraded with respect to the thermionic limit of 60 mV/dec. This is a direct consequence of the carrier energy relaxation due to phonon emission, which allows the interband electron transmission at the channel-drain interface also when the top of the valence band in the middle of the channel is

pushed below the lower edge of the NbS<sub>2</sub> band. This effect is illustrated in Fig. 3e, which reports the current spectral density when the device operates in the subthreshold region.

In Fig. 4a we explore the scaling behavior of the transistor. Transfer characteristics are almost overlapping for  $L_G > 10$  nm, while significant performance degradation are observed for  $L_G = 5$  nm. Particularly, the subthreshold swing increases to  $\sim 250$  mV/dec and the  $I_{ON}/I_{OFF}$  ratio correspondingly drops to 740 and 300 for  $V_{DS} = -0.8$  V and  $V_{DS} = -0.6$  V, respectively (see Table II). Also, the output resistance undergoes a large decrease, settling to  $\sim 12$  k $\Omega \cdot \mu\text{m}$  at  $V_{DS} = V_{GS} = -0.6$  V (see Fig. 4b). The performance drop can be traced back to a strongly reduced capability of the gates to modulate the channel potential, as illustrated in panel Fig. 4c. Quantitatively, for  $L_{ch} = 5$  nm the gate efficiency reduces to 0.57. Another marker of performance degradation as the channel length shrinks, is the threshold voltage roll-off  $\Delta V_T$  with respect to the  $L_{ch} = 20$  nm case, which is reported in Table III for the other considered values of  $L_{ch}$ .

TABLE II:  $I_{ON}/I_{OFF}$  at  $V_{DS} = -0.6$  and  $-0.8$  V ratio for different channel lengths.

$V_{DS}$ [V]	$L_{ch}$ [nm]	$I_{ON}/I_{OFF}$
-0.6	5	300
-0.6	10	1180
-0.6	15	1280
-0.6	20	1290
-0.8	5	740
-0.8	10	2130
-0.8	15	2300
-0.8	20	2330

TABLE III: Threshold voltage roll-off  $\Delta V_T$  for different channel lengths.

$L_{ch}$ [nm]	$\Delta V_T$ [V]	$\Delta V_T$ [V]
	@ $V_{DS} = -0.6$ V	@ $V_{DS} = -0.8$ V
5	0.16	0.25
10	0.02	0.05
15	0.01	0.03

The effect of gate overlaps and underlaps on the  $I_{ON}/I_{OFF}$  ratio for  $L_{ch} = 15$  nm is reported in Table IV. As one expects, the presence of overlaps has the effect of improving the  $I_{ON}/I_{OFF}$  ratio, as it results in a better electrostatic control over the channel potential. On the contrary, the presence of underlaps is detrimental to the device performance. More importantly, a comparison between Table II and Table IV highlights that the impact of the gate overlap (underlap) is much stronger than an equivalent gate extension (reduction) with  $\delta = 0$ . For instance, an increase of  $L_G$  from 10 nm to 15 nm by symmetrically including 2.5 nm-long overlaps on the

source and drain sides, results in a 30% improvement of the  $I_{ON}/I_{OFF}$  ratio, while an equivalent extension of  $L_G$  with  $\delta = 0$  only results in a 8% improvement. Analogously, a decrease of  $L_G$  from 15 nm to 10 nm by symmetrically including 2.5 nm-long underlaps on the source and drain sides degrades the  $I_{ON}/I_{OFF}$  ratio by 48%, while an equivalent gate shrinking with  $\delta = 0$  only yields a 8% reduction. This is a consequence of the modulating effect of the gate over the Schottky barrier thickness already highlighted in Fig. 3b. When  $V_{GS}$  decreases, more holes are induced in the MoS<sub>2</sub> channel, leading to a reduction in the size of the depletion regions associated with the Schottky barriers; this results in a thinning effect on the barriers themselves. In the presence of gate overlaps, the gate is more effective in inducing charge close the NbS<sub>2</sub>/MoS<sub>2</sub> interfaces and therefore in thinning the barriers and modulating the current. Finally, in order to

TABLE IV:  $I_{ON}/I_{OFF}$  for  $L_{ch} = 15$  nm at different gate overlap/underlap.

$V_{DS}$ [V]	$\delta$ [nm]	$I_{ON}/I_{OFF}$
-0.6	-2.5	670
-0.6	0.0	1280
-0.6	2.5	1540
-0.8	-2.5	1299
-0.8	0.0	2300
-0.8	2.5	2630

comprehensively evaluate the potential of the device, we analyze several dynamic performance metrics that are relevant to a wide range of technological applications. These metrics include the intrinsic delay time ( $\tau$ ), the power-delay product (PDP) and the cut-off frequency ( $f_t$ ). The intrinsic delay time and power-delay product are the basic figures of merit in digital applications, while the cut-off frequency characterizes the device with respect to radiofrequency applications.

$\tau$  and PDP are calculated in a quasi-static approximation using the equations [24]

$$\tau = \frac{Q_{ON} - Q_{OFF}}{I_{ON}}, \quad (3)$$

$$\text{PDP} = (Q_{ON} - Q_{OFF})|V_{DS}|, \quad (4)$$

where  $Q_{ON}$  and  $Q_{OFF}$  are the total charge in the channel in the ON and OFF states, respectively. The cut-off frequency  $f_t$  is evaluated as [24]

$$f_t = \frac{1}{2\pi} \frac{g_m}{C_G} \Big|_{\max(g_m)} \quad (5)$$

where  $C_G = \partial Q_{ch}/\partial V_G$  is the total capacitance seen from the gates and  $g_m = \partial I/\partial V_G$  is the transistor transconductance. The results are shown in Fig. 5 as a function of the channel length  $L_{ch}$ .

The intrinsic delay time as a function of  $L_{ch}$  is shown in Fig. 5a. For  $L_{ch} > 5$  nm and  $\delta = 0$ , the intrinsic delay

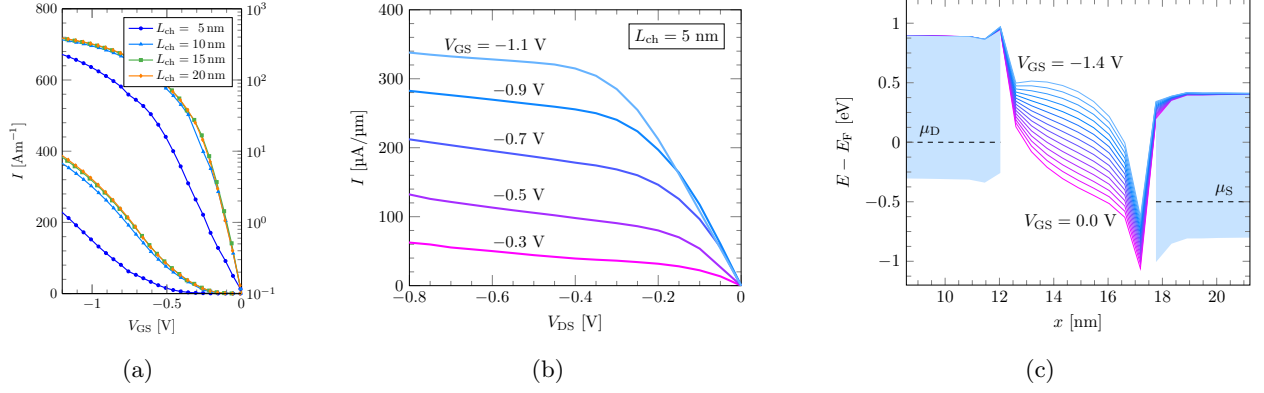


FIG. 4: (a) Transistor transfer characteristics for different channel lengths  $L_{ch} = 5, 10, 15, 20$  nm. (b) Output characteristics for  $L_{ch} = 5$  nm. (c) Band diagram at  $L_{ch} = 5$  nm for several values of  $V_{GS}$ , at  $V_{DS} = -0.5$  V.

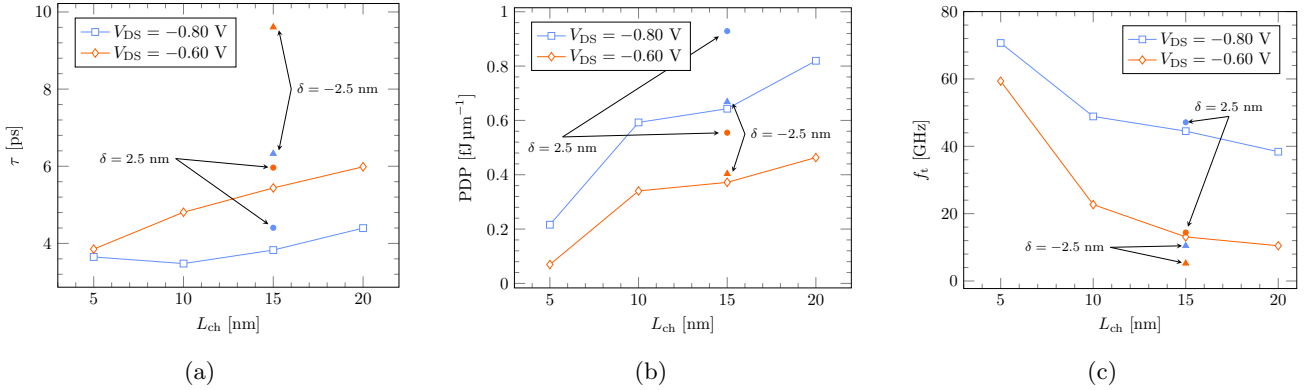


FIG. 5: Dynamic figures of merit of the transistor as a function of the channel length for  $V_{DS} = -0.6$  V and  $-0.8$  V. (a) Intrinsic delay time. (b) Power-delay product. (c) Cut-off frequency. In all the cases, the results for a gate overlap (underlap) with  $\delta = 2.5$ nm ( $\delta = -2.5$ nm) at  $L_{ch} = 15$  nm are also shown.

time decreases approximately linearly with  $L_G$ . Larger deviations from this behavior are observed for  $L_{ch} = 5$  nm, as the values of  $\tau$  for  $V_{DS} = -0.6$  and  $-0.8$  V approximately converge toward a common value of 3.8 ps. The dependence on  $\delta$  is quantified for  $L_{ch} = 15$  nm. A large increase of  $\tau$  with respect to the case  $\delta = 0$  is observed for  $\delta = -2.5$ , due to the previously discussed  $I_{ON}$  degradation.

The power-delay product showed in Fig. 5b increases with increasing  $V_{DS}$  and  $L_{ch}$ , according to Equation (4). A significant increase is observed in the presence of gate overlaps, which indirectly causes an increase of  $Q_{ON}$  by enhancing the coupling between the channel and the contacts.

At fixed  $V_{DS}$ , the cutoff frequency showed in Fig. 5c follows a  $1/C_G \propto 1/L_{ch}$  behavior. Increasing  $V_{DS}$  entails an increase of  $g_m$  and, in turn, an increase of  $f_t$ . In the presence of gate underlaps, the dependence of the transconductance on  $V_{DS}$  becomes much weaker and  $f_t$  tends to settle to a common value of  $\sim 10$  GHz.

## IV. CONCLUSIONS

The possibility to fabricate *p*-type field-effect transistors based on 2D materials is essential to develop a CMOS process based on 2D materials. Following recent experimental demonstrations, we have modeled and numerically simulated a *p*-type transistor based on lateral heterojunctions of  $\text{MoS}_2$  and  $\text{NbS}_2$  monolayers. The metallic  $\text{NbS}_2$  regions act as source and drain extensions, mediating between the  $\text{MoS}_2$  channel and the 3D metal contacts of source and drain. Our results indicate that the performance of the device is strongly dependent on the modulation of the Schottky barriers at the  $\text{MoS}_2/\text{NbS}_2$  interfaces as a function of both the gate voltage and the drain-to-source bias. In this respect, the gate length and the gate alignment with the  $\text{MoS}_2/\text{NbS}_2$  interfaces prove to be critical parameters to optimize the device performance. These geometrical considerations are expected to have a broader applicability and to describe some general tradeoffs in the design of lateral heterojunction field-effect transistors based on two-dimensional materials. The scaling behavior shows a strong reduction of the  $I_{ON}/I_{OFF}$  ratio at channel lengths of 5 nm, while the dynamic fig-

ures of merit remain dominated by capacitive effects and generally improve as the channel shrinks.

## V. ACKNOWLEDGEMENTS

This work was partially supported by the European Union Horizon 2020 Framework Programme under the

“Quantum Engineering for Machine Learning” (QUE-FORMAL) project (Grant Agreement No. 829035), by the by the Italian MIUR through the PRIN project FIVE2D and by the Italian Ministry of University and Research through the ForeLab Departments of Excellence Grant

- 
- [1] J. Tersoff, *Phys. Rev. Lett.* **52**, 465 (1984).
- [2] L. Yang, K. Majumdar, H. Liu, Y. Du, H. Wu, M. Hatzistergos, P. Y. Hung, R. Tieckelmann, W. Tsai, C. Hobbs, and P. D. Ye, *Nano Letters* **14**, 6275 (2014), pMID: 25310177, <https://doi.org/10.1021/nl502603d>.
- [3] A. Allain, J. Kang, K. Banerjee, and A. Kis, *Nature Materials* **14**, 1195 (2015).
- [4] D. Jena, K. Banerjee, and G. H. Xing, *Nature Materials* **13**, 1076 (2014).
- [5] N. Kaushik, D. Karmakar, A. Nipane, S. Karande, and S. Lodha, *ACS Applied Materials & Interfaces* **8**, 256 (2016), pMID: 26649572, <https://doi.org/10.1021/acsami.5b08559>.
- [6] L. Xie, M. Liao, S. Wang, H. Yu, L. Du, J. Tang, J. Zhao, J. Zhang, P. Chen, X. Lu, G. Wang, G. Xie, R. Yang, D. Shi, and G. Zhang, *Advanced Materials* **29**, 1702522 (2017), <https://onlinelibrary.wiley.com/doi/pdf/10.1002/adma.201702522>.
- [7] D. S. Schulman, A. J. Arnold, and S. Das, *Chem. Soc. Rev.* **47**, 3037 (2018).
- [8] X. Cai, Z. Wu, X. Han, Y. Chen, S. Xu, J. Lin, T. Han, P. He, X. Feng, L. An, R. Shi, J. Wang, Z. Ying, Y. Cai, M. Hua, J. Liu, D. Pan, C. Cheng, and N. Wang, *Nature Communications* **13**, 1777 (2022).
- [9] S. Chen, S. Wang, C. Wang, Z. Wang, and Q. Liu, *Nano Today* **42**, 101372 (2022).
- [10] M. S. Choi, N. Ali, T. D. Ngo, H. Choi, B. Oh, H. Yang, and W. J. Yoo, *Advanced Materials* **34**, 2202408 (2022), <https://onlinelibrary.wiley.com/doi/pdf/10.1002/adma.202202408>.
- [11] D. S. Schneider, E. Reato, L. Lucchesi, Z. Wang, A. Piccietini, J. Bolten, D. Marian, E. G. Marin, A. Radenovic, Z. Wang, G. Fiori, A. Kis, G. Iannaccone, D. Neumaier, and M. C. Lemme, in *2021 Device Research Conference (DRC)* (2021) pp. 1–2.
- [12] C. Kim, I. Moon, D. Lee, M. S. Choi, F. Ahmed, S. Nam, Y. Cho, H.-J. Shin, S. Park, and W. J. Yoo, *ACS Nano* **11**, 1588 (2017), pMID: 28088846, <https://doi.org/10.1021/acs.nano.6b07159>.
- [13] Y. Wang, J. C. Kim, R. J. Wu, J. Martinez, X. Song, J. Yang, F. Zhao, A. Mkhoyan, H. Y. Jeong, and M. Chhowalla, *Nature* **568**, 70 (2019).
- [14] X. Liu, M. S. Choi, E. Hwang, W. J. Yoo, and J. Sun, *Advanced Materials* **34**, 2108425 (2022), <https://onlinelibrary.wiley.com/doi/pdf/10.1002/adma.202108425>.
- [15] Y. Zhang, L. Yin, J. Chu, T. A. Shifa, J. Xia, F. Wang, Y. Wen, X. Zhan, Z. Wang, and J. He, *Advanced Materials* **30**, 1803665 (2018), <https://onlinelibrary.wiley.com/doi/pdf/10.1002/adma.201803665>.
- [16] P.-C. Shen, C. Su, Y. Lin, A.-S. Chou, C.-C. Cheng, J.-H. Park, M.-H. Chiu, A.-Y. Lu, H.-L. Tang, M. M. Tavakoli, G. Pitner, X. Ji, Z. Cai, N. Mao, J. Wang, V. Tung, J. Li, J. Bokor, A. Zettl, C.-I. Wu, T. Palacios, L.-J. Li, and J. Kong, *Nature* **593**, 211 (2021).
- [17] Q. He, Y. Liu, C. Tan, W. Zhai, G.-h. Nam, and H. Zhang, *ACS Nano* **13**, 12294 (2019), publisher: American Chemical Society.
- [18] Z. Wang, M. Tripathi, Z. Golsanamlou, P. Kumari, G. Lovarelli, F. Mazziotti, D. Logoteta, G. Fiori, L. Sementa, G. M. Marega, H. G. Ji, Y. Zhao, A. Radenovic, G. Iannaccone, A. Fortunelli, and A. Kis, *Advanced Materials* **35**, 2209371 (2023).
- [19] S. Datta, in *Digest. International Electron Devices Meeting*, (2002) pp. 703–706.
- [20] W. Lee, N. Jean, and S. Sanvito, *Phys. Rev. B* **79**, 085120 (2009).
- [21] X. Li, J. T. Mullen, Z. Jin, K. M. Borysenko, M. Buongiorno Nardelli, and K. W. Kim, *Phys. Rev. B* **87**, 115418 (2013).
- [22] Z. Jin, X. Li, J. T. Mullen, and K. W. Kim, *Phys. Rev. B* **90**, 045422 (2014).
- [23] “More moore tables. international roadmap for devices and systems (irds),” <https://irds.ieee.org/editions/2021> (2021), accessed: 2023-10-04.
- [24] F. Mazziotti, D. Logoteta, and G. Iannaccone, *Phys. Rev. Appl.* **17**, 014011 (2022).